PHYSICAL REVIEW B **70**, 184419 (2004)

Interfacial strain measurements of $SrRuO_3/SrMnO_3$ magnetic multilayers

P. Padhan, W. Prellier,* and B. Mercey
Laboratoire CRISMAT, CNRS UMR 6508, ENSICAEN, 6 Bd du Maréchal Juin, F-14050 Caen Cedex, France

(Received 26 April 2004; revised manuscript received 23 June 2004; published 12 November 2004)

Magnetic multilayers of $(SrRuO_3)_m(SrMnO_3)_n$ were grown artificially using the pulsed-laser deposition technique on (001)-oriented $SrTiO_3$ substrates. The state of strain at the interfaces and the structural coherency are studied in details utilizing asymmetrical x-ray diffraction and the $\sin^2 \psi$ method. First, the evolution of the lattice parameters and the crystallinity and epitaxy of the films are evaluated as a function of the number of $SrMnO_3$ unit cells using x-ray diffraction and transmission electron microscopy. Second, our results on the stress indicate that the $SrRuO_3/SrMnO_3$ superlattices show a larger residual strain as compared to the single-layer film of $SrRuO_3$. This suggests a lattice stiffening from interfacial strain, which inhibits the dislocation by composition modulation. Finally, these results bring insights into the interfacial stress measurements of oxide multilayers that can be used to control the physical properties at the level of the atomic scale.

DOI: 10.1103/PhysRevB.70.184419 PACS number(s): 75.70.−i, 68.60.Bs, 75.47.Gk, 61.10.Nz

Magnetic multilayer structures based on transition metals[1,2] and their compounds[1–14] have high potential for technological applications as their transport and magnetic properties can be controlled with the nonmagnetic spacer layer thickness. However, to use these materials for applications, it is necessary to understand and control precisely the physical properties that depend on various parameters such as the layer materials, their thicknesses, and the interfaces between them. In the case of magnetic multilayers, the interfaces are rich in magnetic and structural coordinations. Moreover, the lattice mismatch and thickness between the two constituent materials will also modify the strength of the interfaces. Furthermore, the lattice-mismatch-induced strain changes the physical properties of the oxide thin films, including the transition temperature in high-temperature superconductors[15,16] and in ferroelectric oxides.[17] A similar effect in the Mn-based multilayers is responsible for significant variation in magnetization as well as in electronic, transport, and structural properties.[13,14,18] For example, Kreisel *et al.*[19] have observed a tensile-strain-induced rhombohedral-to-orthorhombic phase transition in $La_{0.7}Sr_{0.3}MnO_3/SrTiO_3$ by Raman scattering. In this system, these two phases $La_{0.7}Sr_{0.3}MnO_3$ and $SrTiO_3$ coexist in the superlattice with an intermediate range of layer thickness. Lue and co-workers[10] have also studied the structural and transport properties of $La_{2/3}Ba_{1/3}MnO_3/SrTiO_3$ structure. They observed that electrical transport properties of these samples strongly depend on the strain-induced distortion in the $La_{2/3}Ba_{1/3}MnO_3$ layer.

Considering the above points, it is interesting first to fabricate magnetic multilayers using thin-film deposition processes. Second, artificial control of their properties as a function of the spacer layer thickness is required. Third, the interfacial stress that plays an important role upon the structural and magnetotransport properties needs to be evaluated.

In this article, we report a structural study of the superlattices consisting of 20-unit-cell- (u.c.-) thick $SrRuO_3$ (SRO) and n-u.c.-thick $SrMnO_3$ (SMO) where n varies from 1 to 20 grown on (001)-oriented $SrTiO_3$ (STO, cubic with $a = 3.905$ Å). We choose these materials because SRO is a ferromagnetic metal[20] whereas SMO is a highly insulating antiferromagnet.[21] Moreover, the lattice parameter of bulk SRO ($a_{SRO} = 3.93$ Å) is larger than a_{STO} with a lattice mismatch +0.6% whereas the lattice parameter of SMO ($a_{SMO} = 3.805$ Å) is smaller than a_{SRO} with lattice mismatch −3.0%. Though there is a large lattice mismatch between SRO and SMO, we have chosen this combination because the *A*-site ions are the same and the reduction of *B*-site distortion[22] is expected at the interfaces between SRO and SMO. The state of strain at the interfaces and the structural coherency are studied using the $\sin^2 \psi$ method, and our results are reported in this article. The superlattices show larger residual strain compared to the single-layer film of SRO, suggesting that a lattice stiffening from interfacial strain and inhibiting dislocation by composition modulation.

A multitarget pulsed laser deposition system[16] was used to grow SRO thin films and SRO/SMO superlattices on (001) $SrTiO_3$ substrates. The thin films of SRO and the superlattices were deposited at 720 °C in oxygen ambient of 30 mtorr. The deposition rates (typically ~ 0.26 Å/pulse) of SRO and SMO were calibrated for each laser pulse of energy density $\sim 3\ \mathrm{J/cm^2}$. After the deposition the chamber was filled to 300 torr of oxygen at a constant rate, and then the samples were slowly cool down to room temperature at the rate of 20 °C/min. The superlattice structures were synthesized by repeating 15 times the bilayer comprising of 20 u.c. SRO and n u.c. SMO. In all samples SRO is the bottom layer, and the modulation structure was covered with 20 u.c. SRO to keep the structure of the top SMO layer stable. These periodic modulations in composition, created on the basis of established deposition rates of SRO and SMO, were confirmed from the positions of superlattice reflections in x-ray θ-2θ scans. The epitaxial growth and the structural characterization of the multilayer and single-layer films were performed using x-ray diffraction, electron dispersive spectroscopy (EDS), and transmission electron microscopy (TEM). The θ-2θ, Φ, and ω scans were performed using Seifert XRD 3000P and Philips MRD X'pert diffractometers ($\lambda = 1.540\,69$ Å). The TEM is a JEOL 2010 with a point resolution of 1.8 Å. Resistivity (ρ) was measured as a function of temperature (T) in PPMS Quantum Design.

1098-0121/2004/70(18)/184419(7)/$22.50 ©2004 The American Physical Society

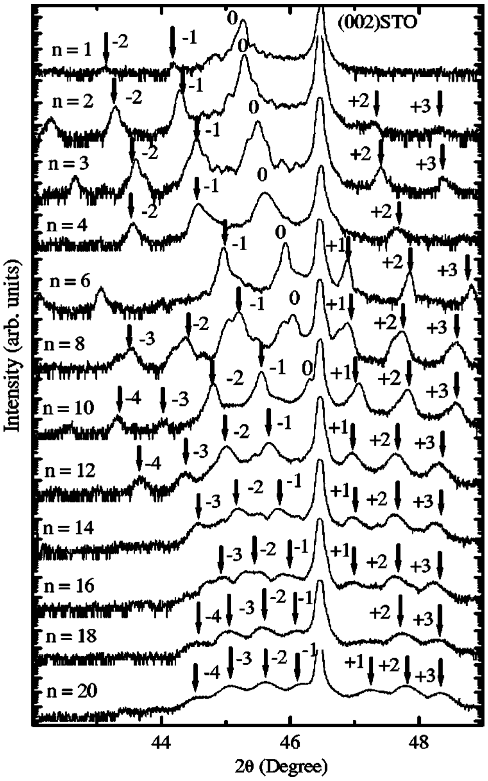

FIG. 1. Θ-2Θ scan recorded around the 002 reflection of STO for various multilayer $(SRO)_{20}(SMO)_n$ $(n=1-20)$. Note the presence of satellites peaks (denoted by arrows) of several orders (from −3 to +3) around the main (fundamental) peak (order 0) attesting to the formation of superlattices.

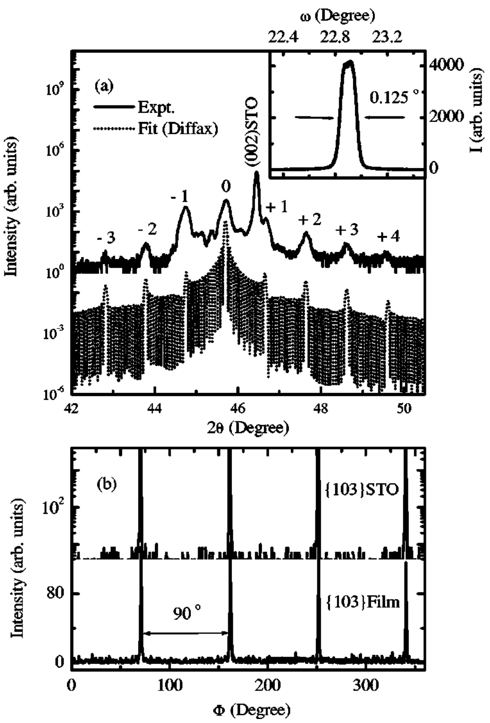

FIG. 2. (a) Θ-2Θ scan around the 002 reflection of STO for a multilayer $(SRO)_{20}(SMO)_5$. The calculated intensity using the DIFFAX program is also indicated. Note the perfect agreement between experimental and calculated intensities. The inset depicts the ω scan recorded around the main peak for the same film. The low value of the FWHM close to 0.12° confirms the high quality of the superlattice. (b) Φ scans recorded around the {103} of the film and the STO substrate showing a fourfold symmetry and an in-plane alignment.

In bulk form SRO exhibits only pseudocubic perovskite structure.[20] In contrast, stoichiometric SMO crystallizes in a cubic as well as hexagonal phase.[23] The cubic perovskite structure of SMO is not stabilized in its single-layer thin-film form; however, our results of x-ray diffraction and transmission electron microscopy show the formation of cubic perovskite structure of SMO layer in the superlattices as previously observed.[18,23] This result indicates that SMO can be stabilized as a cubic structure between two SRO layers.[24]

Our samples with alternate layers of SRO and SMO on STO show $(00l)$ diffraction peaks of the constituents, indicating the growth of an epitaxial pseudocubic phase with the c-axis orientation—i.e., the c axis perpendicular to the substrate plane. In Fig. 1, we show the θ-2θ scan for several samples with different spacer layer thicknesses. These scans are around the (002) reflection (42°–49° in 2θ) of these pseudocubic perovskites. As the SMO layer thickness increases above 1 u.c., the fundamental (002) diffraction peak of the constituents shifted towards the angular position of the STO and overlapped it for $n > 10$. The sample with $n=1$ shows two weak satellite peaks on the lower-angle side of the (002) diffraction peak of the constituents. The presence of higher-order strong satellite peaks on either side of the (002) diffraction peak for samples with $n \geqslant 2$ clearly indicates the formation of a new structure having a periodic chemical modulation of the constituents.

In SRO/SMO superlattices, the two constituents have perovskite structure and the difference in the lattice parameters between them is significant (3.93 Å vs 3.805 Å). Also the atomic scattering factor of Ru is higher than Mn. Higher-order satellite peaks with strong intensity are expected to be observed in the x-ray diffraction. To extract information about the coherency at the interfaces and the periodic chemical modulation (Λ) of these superlattices from θ-2θ scans, we have carried out a quantitative refinement of the superlattice structure using the DIFFAX program.[25] The experimental and simulated diffraction profiles of the sample with $n=5$ are shown in Fig. 2(a). It shows only the 2θ range close to the fundamental (002) reflection (42°–51° in 2θ). The simulated profile is in good agreement with the measured θ-2θ scan with respect to the satellite peak position and relative intensity ratio. The inset in Fig. 2(a) shows the rocking curve (ω scan) recorded around the fundamental (002) diffraction peak of the sample with $n=5$. The full width at half maximum (FWHM) of the rocking curve is 0.125°, close to the instrumental limit, suggesting a high crystalline quality of the structure in the samples. The FWHM of the rocking curve also correlates the structural coherence length ξ of the sample with the relation $\xi = 2\pi/Q \times \text{FWHM}$ (Ref. 26), where $Q(\approx 1/d)$ is the scattering vector length and the FWHM is in radians. The coherence length of the sample in the out-of-plane direction is nearly the same as the total thickness of the multilayer structure, confirming the coherency and single crystallinity of the samples.

An asymmetric diffractometer configuration provides a quantitative measure of the in-plane coherency, pseudomorphic growth, and stress in all three directions. In this configuration, the Φ scan of the sample with $n=5$ from the asymmetric $\{103\}$ planes is shown in Fig. 2(b). The Φ scans of the substrate and film correspond to the angular position of the substrate and the constituents in the θ-2θ scan at asymmetric $\{103\}$ planes. The presence of symmetric and periodic peaks with a period of 90° confirms the fourfold symmetry of these pseudocubic perovskites. The negligibly small difference between the angular position of the peak (in the Φ scan) of the substrate and film clearly shows the cube-on-cube growth morphology of the film. The in-plane alignment is as follows: $[100]_{\mathrm{STO}}//[100]_F$ and $[010]_{\mathrm{STO}}//[010]_F$ (where the index F refers to the film).

The quality of the superlattices is confirmed by the electron diffraction (ED) study. An example of an ED cross section, for a $(\mathrm{SRO})_{20}\,(\mathrm{SMO})_5$ superlattice, is given in Fig. 3(a). Note that the ED is a superposition of SRO and SMO. The perfect ED patterns confirms the c-axis orientation of the superlattice and, also, the perovskite structure. Moreover, the satellite spots [see inset of Fig. 3(a)], due to the periodic stacking of the SRO and SMO layers, are clearly visible. The corresponding cross-section high-resolution electron microscopy (HREM) image is shown in Fig. 3(b). It confirms the presence of superstructure and sharp heteroepitaxial SRO-SMO interfaces. The image also indicates that the SMO perovskite type is stabilized between two SRO layers and, actually, adopts a pseudocubic structure.[24]

Having the epitaxial and pseudocubic growth morphology, it is necessary to verify the periodicity of all samples with different spacer layer thickness. In (20 u.c.) SRO/(n u.c.) SMO structure, the average superlattice period is

$$\frac{\Lambda}{20+n}=\left(\frac{20a_{\mathrm{SRO}}+na_{\mathrm{SMO}}}{20+n}\right)=\left(\frac{20a_{\mathrm{SRO}}+na_{\mathrm{SMO}}}{N}\right), \quad (1)$$

where $N=20+n$. Since the fundamental diffraction peak of the superlattice is due to the diffraction from the constituent, we have assumed the lattice parameter of the superlattice (a) as $a\simeq(a_{\mathrm{SRO}}+a_{\mathrm{SMO}})/2$. The superlattice period can be expressed as

$$\Lambda \simeq (20+n)a. \quad (2)$$

.

For higher spacer layer thickness (i.e., $n=20$) the superlattice period is $\simeq$156 Å. This suggests that the coherence length of the sample is much higher than the superlattice period. Therefore, the higher angle satellite peak positions[27] can be indexed about a, $(2\sin\theta)/\lambda=1/a\pm n/\Lambda$, where θ is the angular position of the satellite peak and λ is the x-ray wavelength. We used the following equation[27] to extract the superlattice period from the satellite peak positions in the θ-2θ scan:

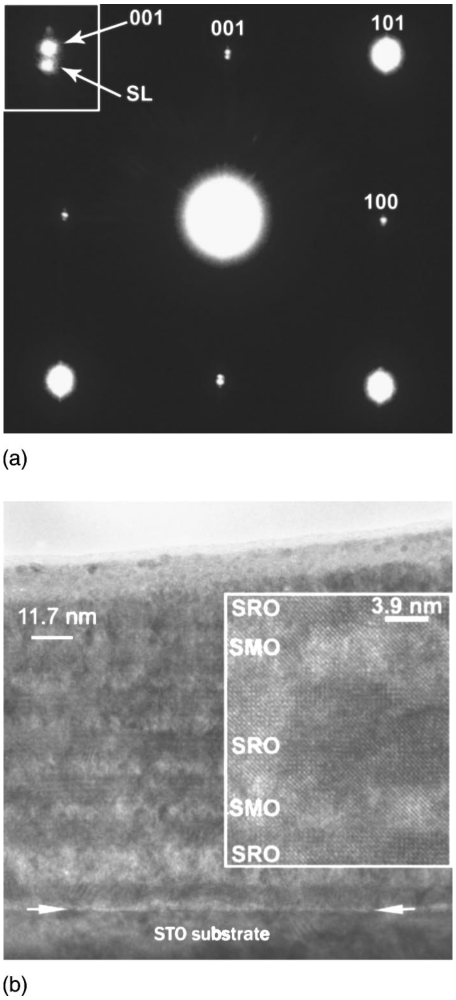

FIG. 3. (a) Electron diffraction of a cross-section for a $(\mathrm{SRO})_{20}(\mathrm{SMO})_5$ multilayer taken along the [010] direction. The inset is the enlargement of the 001 spot showing one satellite spot (SL) resulting from the superstructure. (b) Overall cross-section image showing the STO substrate and the superlattice $(\mathrm{SRO})_{20}(\mathrm{SMO})_5$. The inset is an enlargement showing the stacking. The SRO and SMO layers are clearly visible. The arrows indicate the substrate-film interface.

$$\Lambda=\frac{\lambda}{2(\sin\theta_i-\sin\theta_{i+1})}, \quad (3)$$

where θ_i and θ_{i+1} are the angular position of the ith- and $(i+1)$th-order satellite peak, respectively. The calculated values of Λ from the different successive satellite peak positions are given in Fig. 4(a) for different values of n. The superlattice period is linear with n and follows Eq. (2), indicating a high quality of the different samples and a clear correlation as a function of the spacer layer thickness.

As previously stated, the physical properties of magnetic thin films (Mn-based system) are strongly dependent on the strains imposed by the substrate.[28] This dependence has also been reported in the case of SRO thin films[29] where a_{SRO} is larger than a_{STO} which indicates the presence of compressive in-plane stress on the SRO film. The substrate-induced stress

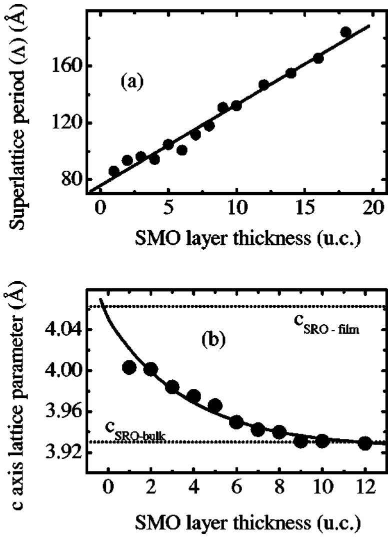

FIG. 4. (a) Evolution of the superlattice period (Λ) as a function of the number of SMO layer calculated from the position of the satellite peaks of Fig. 1 (see text for details). The solid line is the fit to the data. (b) Evolution of the average *c*-axis lattice parameter $[=\Lambda/(20+n)]$ as a function of the number of SMO layers, calculated from the position of the satellite peaks of Fig. 1 (see text for details). The line is only a guide for the eyes. The *c*-axis value of the bulk SRO as well as the *c*-axis value obtained for a 20-u.c.-thick SRO film are also indicated for comparison.

modifies the interatomic distance in SRO and this is maximum close to the STO substrate. However, the substrate-induced stress relaxed as the number of SRO layers increases. This is evidenced when the lattice parameter of SRO approaches to bulk value. Since a_{SMO} is smaller than a_{SRO}, the SMO layer on SRO will experience a tensile strain within the plane. Consequently, the strain of the SRO/SMO superlattices is a combined effect of substrate-induced strain as well as the strain originated from the interfaces.

In this superlattice system, these strains are opposite in nature (substrate-induced strain is compressive, whereas the strain at the interfaces is tensile). Also the lattice parameter calculations suggest that the interfacial strain is larger compared to the substrate-induced strain. So it is important to understand both the influence of strain on the lattice parameter of this structure and the influence of the SMO layer thickness upon the strain. In Fig. 4(b), we report the average out-of-plane lattice parameter of various samples as a function of spacer layer thickness. The out-of-plane lattice parameter of 20-u.c.-thick SRO on STO is 4.05 Å, while it is 4.003 Å for the superlattice with 1 u.c. spacer layer. From the figure, we observed that as the spacer layer thickness increases, the out-of-plane lattice parameter of the superlattice decreases and approaches the bulk value of SRO, which indicates a smooth relaxation of the strain within the film.

In the transition metal multilayers each layer of the constituent has a single element where the lattice mismatch leads to a planar deformation at the interfaces and hence its structure. While in a multilayer designed from various transition metal compounds, the lattice mismatch introduces a deformation in the three-dimensional (3D) coordination of the transition metal element. To understand the structural correlation of this SRO/SMO system at the interfaces, we have studied the asymmetric reflection of these samples using the conventional $\sin^2\psi$ method[30] (where ψ is the angle between the lattice plane normal and the sample surface normal). This method is commonly used to calculate Poisson's ratio (ν), in-plane and out-of-plane strain, and the strain free lattice parameter of the films. The lattice mismatch between the deposited material and the substrate is the source of strain in epitaxial thin film. In addition, the strain (ε) of the film along the direction of diffraction $[hlk]$ from any hkl reflection for a biaxial strain state is defined as[30]

$$\varepsilon=\frac{d_{hkl}(\phi\psi)-d_0}{d_0}=\varepsilon_{11}-\varepsilon_{33}\sin^2\psi+\varepsilon_{33}, \tag{4}$$

where ϕ is the angle between the projected lattice plane normal and an in-plane axis. The parameters $d_{hkl}(\phi\psi)$ and d_0 are the strained and unstrained (i.e., bulk value) (hkl) plane spacing of the sample, respectively. $\varepsilon_{11}=\varepsilon_{22}$ are the in-plane strain components and ε_{33} is the out-of-plane strain component in the film. The values of d_0 and ε_{ii} $(i=1,2,3)$ depend on the elastic constant (or Young's modulus E) and ν.

We have chosen a unique direction with constant h and k to measure the diffracted x-ray intensity as well as ψ from the $10l$ $(l=1,2,3$, and 4) asymmetric reflection. The value of ψ is sensitive to the alignment of the sample, and to avoid the misaligned contribution of ψ, we have averaged over all ϕ directions. In Fig. 5(a) we show the $d_{10l}(\phi\psi)$ vs $\sin^2\psi_{10l}$ plot for two samples ($n=1$ and $n=12$). The values are similar for both samples whose strain-free lattice parameter of the bilayer is expected to be different. From the experimental viewpoint the values of ψ are also expected to be the same for a known plane in each sample.

Assuming the same strain-free lattice parameter for all samples, we have calculated the in-plane and out-of-plane strain from the $d_{10l}(\phi\psi)$ vs $\sin^2\psi_{10l}$ plot. We have determined the value of d_0 from the Fig. 5(a) at $\sin^2\psi_0=2\nu/(1+\nu)$, using the ν value ($\nu=0.327$ in agreement with previous reports on manganite thin films[31]) calculated from the [111] direction. The value of ν was calculated using the relation[30]

$$\left(\frac{a_F-a_{\mathrm{STO}}}{a_F}\right)=\left(\frac{c_F-c_{\mathrm{STO}}}{c_F}\right)\left(\frac{1-\nu}{1+\nu}\right), \tag{5}$$

where a_F and c_F are the *a*-axis and *c*-axis lattice parameters of the film ($a_{\mathrm{STO}}=c_{\mathrm{STO}}=3.905$ Å). These values a_F and c_F are calculated from the [111] direction for the multilayer with $n=1$. Using this value of d_0 in Eq. (4), we have calculated the strain components for different samples are shown in Fig. 5(b). The ε_{11} and ε_{33} are opposite in nature and the in-plane strain is stronger as expected from lattice parameter considerations. From this figure, we found that the strain is independent of the superlattice period although the out-of-plane lattice parameter shows relaxation of the stress at higher spacer layer thickness [see Fig. 4(b)]. However, this analysis does not make a distinction between the strain in the multilayer and the single-layer SRO film. Also the (111) diffraction peak of the sample overlaps with that of the substrate peak which prohibits calculating d_0 of each sample.

Equation (4) is applicable for a thin film where the struc-

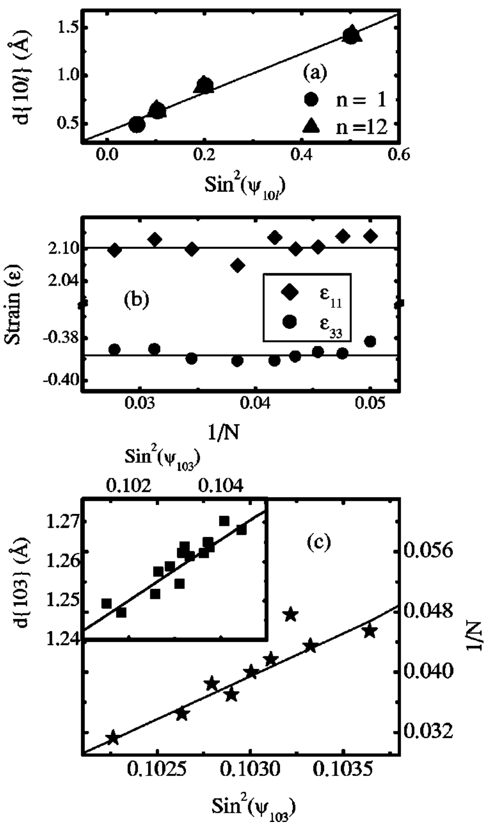

FIG. 5. (a) d_{10l} vs $\sin^2\psi_{10l}$ ($l=1,2,3,$ and 4) for $(\mathrm{SRO})_{20}(\mathrm{SMO})_n$ with $n=1$ and $n=12$. The solid line is a fit to the data. (b) Evolution of the in-plain strain (ε_{11}) and out-of-plane strain (ε_{33}) as a function of the inverse of the bilayer unit cell ($1/N$). The line is only a guide for the eyes. (c) Evolution of the inverse of the bilayer unit cell ($1/N$) as a function of $\sin^2\psi_{103}$. The inset depicts the evolution of d_{103} vs $\sin^2\psi_{103}$ for different multilayers. The solid lines in the figure are the fit to the data.

ture has a single interface between the film and substrate. In the case of a multilayer, which has more than one interface, its lattice parameter depends on the thickness of the bilayer. We have assumed $d_{hkl}(\phi\psi)=a_f/\sqrt{h^2+k^2+l^2}$, where a_f is the average lattice parameter of the bilayer. The average lattice parameter of the bilayer can be expressed as a function of N:

$$a_f = a_{\mathrm{SMO}} + \frac{20}{N}(a_{\mathrm{SRO}} - a_{\mathrm{SMO}}). \tag{6a}$$

Using this value of a_f, Eq. (4) can be written as

$$\frac{[a_{\mathrm{SMO}} + (20/N)(a_{\mathrm{SRO}} - a_{\mathrm{SMO}})]}{\sqrt{h^2 + k^2 + l^2}} = d_0(\varepsilon_{11} - \varepsilon_{33})\sin^2\psi + d_0(\varepsilon_{33} + 1). \tag{6b}$$

To apply this relation to the SRO/SMO multilayer series, we have measured the value of ψ from the 103 asymmetric reflection. The values of $\sin^2\psi_{103}$ for different bilayer thicknesses as a function of ($1/N$) are shown in the Fig. 5(c). The plot shows excellent agreement with Eq. (6b). Using a_{SRO} and a_{SMO} as the bulk value and the value of d_0 calculated from Fig. 5(a), we have calculated the values of strain components. The values of ε_{11} and ε_{33} are 4.0876 and −0.678, respectively. To compare these strain components, we have plotted $d_{103}(\phi\psi)$ with the corresponding $\sin^2\psi_{103}$ for various samples in the inset of Fig. 5(c). The $d_{103}(\phi\psi)$ and $\sin^2\psi_{103}$ of these series satisfy Eq. (4), and the values of ε_{11} and ε_{33} are 4.419 and −0.69, respectively. These values are consistent with the values of strain components calculated from Fig. 5(c). Using the values of $d_0(\varepsilon_{11}-\varepsilon_{33})$ and $d_0(\varepsilon_{33}+1)$ obtained from the inset of Fig. 5(c) and the slope and intercept of Fig 5(c) in Eq. (6b), we have calculated the value of strained lattice parameter of a_{SRO} and a_{SMO} along the 00*l* direction. The values of a_{SRO} and a_{SMO} are 3.99 and 3.864 Å, respectively, confirming the expansion and compression in the out-of-plane direction.

In the SRO/SMO multilayer structure, the out-of-plane direction has alternate stacking of $\mathrm{RuO_6}$ and $\mathrm{MnO_6}$. In a superlattice with $n=1$ the out-of-plane lattice parameter is 4.003 Å which is larger than the lattice parameter of the constituents as well as the substrate. This state of strain indicates the elongation of these octahedra along the *c* axis. This superlattice has a larger strain state compare to the single layer of SRO film, although the total thickness of the structure is larger than a strain-relaxed film [150 Å (Ref. 32)]. The lower strain-relaxed thickness of SRO on STO and larger difference in the lattice parameter between the two compounds of the superlattice suggest that the modulation of bilayer strain is the larger contribution to the total strain in the superlattice. As the bilayer thickness—i.e., as the spacer layer thickness increases—the strain level in the bilayer relaxed and the distortion of these octahedra decreases. This strain at room temperature due to the interfaces is analyzed by $\sin^2\psi$ methods. The strain in Eq. (4) depends on the *hkl* orientations provided the strain is biaxial and uniform. However, Eq. (4) is valid for a thin film with single interfaces and is not restricted to whether the strain is due to the volume conserving modification or not. Thin films of transition metal compounds have been observed to have a strain gradient along the growth direction. The presence of small steps and terraces on the surface of the substrate may also induce nonuniformity in the in-plane strain. This suggest that the value of $\sin^2\psi$ may not follow Eq. (4) for arbitrary *hkl* orientations. For this reason, the samples are studied along 10*l* orientations. The values of strain components are similar to that of the 1000-Å-thick film of SRO on STO seen in Fig. 5(b). In Eq. (4) the parameters that include the stacking nature of the samples are d_0, E, and ν. In the strain calculation, we have used the same d_0 for all samples though the average bilayer lattice parameter is different. This could be the reason that we could not extract any signature of the strain gradient along the 10*l* direction using Eq. (4). Thus, we consider only the 103 direction and compared $d_{103}(\phi\psi)$ with $\sin^2\psi_{103}$ of the samples with different spacer layer thickness [Fig. 5(c)]. The linearly dependent $d_{103}(\phi\psi)$ with $\sin^2\psi_{103}$ for different sample allows us to calculate the strain. The values of the strain components are 2 times larger than the values calculated along the 10*l* direction. Also we have calculated the values of strain components from $\sin^2\psi_{103}$ using Eq. (6b). Both calculations show approximately the same values of strain. The sign of the strain components in the multilayer is

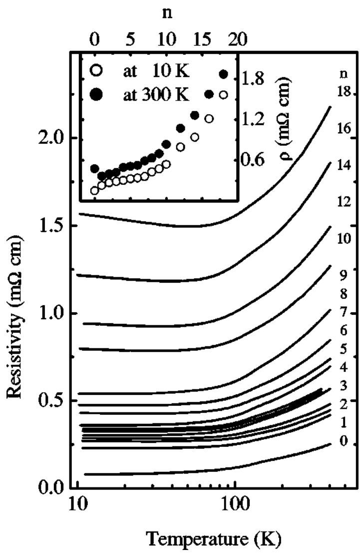

FIG. 6. Temperature-dependent zero-field resistivity for different multilayers. Inset shows the values of zero-field resistivities at 10 and 300 K of these multilayers.

similar to that of the strain components of the SRO thin film. This suggests that the in-plane tensile strain induced in SMO due to 20-u.c.-thick SRO is not so strong as to overcome the substrate-induced strain. The strained out-of-plane lattice parameter of SRO and SMO calculated from Eq. (6) indicates the volume conserving distortion of SRO, whereas the distortion in SMO does not conserve its volume even if it retains its cubic symmetry. At the interfaces, the modified structure of SMO is stabilized in the pseudocubic phase and suppresses the strength of the in-plane tensile strain. In the multilayer the interfaces between the constituents modulate the substrate-induced strain which keeps the strain coherency in the sample. As the bilayer thickness increases, the substrate-induced strain relaxes and it is reflected in the out-of-plane lattice parameter of the multilayer.

The zero-field temperature-dependent resistivity (ρ) of these superlattices is shown in Fig. 6. The resistivity of 1000-Å-thick film of SRO is metal like in the entire temperature range with resistivity anomaly at [150 K (Ref. 20)], while the resistivity of the superlattice with 1-u.c.-thick SMO layer below room temperature is metal like with a resistivity minima at 20 K and below 20 K the resistivity is insulator like. As the SMO layer thickness increases the resistivity minima shifted towards the higher temperature and $\rho(T)$ shows an insulator-to-metal transition. This indicates the presence of an interface effect due to the 3D coordination of Ru and Mn ions, in the $\rho(T)$, though the top layer is a 20-u.c.-thick SRO. The resistivities in the inset of Fig. 6 at 10 and 300 K of these superlattices show a continuous increase in its magnitude with an increase of SMO layer thickness. For the sample with lower SMO layer thickness where the strain is larger [Fig. 4(b)], the change in the magnitude of the resistivity is negligible. Although the transport measurement contains the information of the interfaces, the effect of strain is dominated by the magnetic state of the mobile carrier and the insulating nature of the SMO layer.

In conclusion, we have grown superlattices consisting of 20-u.c.-thick $SrRuO_3$ and n-u.c.-thick $SrMnO_3$ where n varies from 1 to 20 grown on (001)-oriented $SrTiO_3$ utilizing the pulsed-laser deposition technique. The evolution of the lattice parameters, the crystallinity, and the epitaxy of the films are evaluated as a function of the number of $SrMnO_3$ unit cells using x-ray diffraction and transmission electron microscopy. We have also studied the state of strain at the interfaces and the structural coherency using the $\sin^2 \psi$ method. The superlattices show larger residual strain compared to the single-layer film of SRO, suggesting that a lattice stiffening from interfacial strain and inhibiting dislocation by composition modulation. These results bring new insights into the interfacial stress measurements of oxide multilayers that can be used to control the physical properties at the level of the atomic scale.

We thank M. Morin for the preparation of samples for the TEM cross section and J. Lecourt in the targets synthesis. We also thank Dr. H. Eng for careful reading of the article.

We greatly acknowledged financial support of Centre Franco-Indien pour la Promotion de la Recherche Avancee/Indo-French Centre for the Promotion of Advance Research (Grant No.CE-FIPRA/IFCPAR) under Project No. 2808-1.

---

*Electronic address: prellier@ensicaen.fr

[1] B.Y. Jin and J.B. Ketterson, Adv. Phys. **38**, 189 (1989).

[2] *Ultrathin Magnetic Structures I and II*, edited by B. Heinrich and J.A.C. Bland (Springer-Verlag, Berlin, 1994).

[3] G.Q. Gong, A. Gupta, Gang Xiao, P. Lecoeur, and T.R. McGuire, Phys. Rev. B **54**, R3742 (1996).

[4] K. Ueda, H. Tabata, and T. Kawai, Science **280**, 1064 (1998).

[5] M. Izumi, Y. Murakami, Y. Konishi, T. Manako, M. Kawasaki, and Y. Tokura, Phys. Rev. B **60**, 1211 (1999).

[6] Moon-Ho Jo, Neil D. Mathur, Jan E. Evetts, Mark G. Blamire, Manuel Bibes, and J. Fontcuberta, Appl. Phys. Lett. **75**, 3689 (1999).

[7] A. Orozco, S.B. Ogale, Y.H. Li, P. Fournier, Eric Li., H. Asano, V. Smolyaninova, R.L. Greene, R.P. Sharma, R. Ramesh, and T. Venkatesan, Phys. Rev. Lett. **83**, 1680 (1999).

[8] I. Panagiotopoulos, C. Christides, M. Pissas, and D. Niarchos, Phys. Rev. B **60**, 485 (1999).

[9] K.R. Nikolaev, A. Bhattacharya, P.A. Kraus, V.A. Vas'ko, W.K. Cooley, and A.M. Goldman, Appl. Phys. Lett. **75**, 118 (1999).

[10] Yafeng Lu, J. Klein, C. Hofener, B. Wiedenhorst, J.B. Philipp, F. Herbstritt, A. Marx, L. Alf, and R. Gross, Phys. Rev. B **62**, 15 806 (2000).

[11] A. Venimadhav, M.S. Hegde, R. Rawat, I. Das, P.L. Paulose, and E. Sampathkumaran, Phys. Rev. B **63**, 214404 (2001).

[12] J. Verbeeck, O.I. Lebedev, G. Van Tendeloo, and B. Mercey, Phys. Rev. B **67**, 184426 (2002).

[13] P. Padhan and R.C. Budhani, Phys. Rev. B **67**, 024414 (2003).

[14] P. Padhan R.C. Budhani, and R.P.S.M. Lobo, Europhys. Lett. **63**,

771 (2003).

[15] G. Jacob, V.V. Moshchalkov, and Y. Bruynseraede, Appl. Phys. Lett. **66**, 2564 (1995).

[16] W. Prellier, B. Mercey, Ph. Lecoeur, J.F. Hamet, and B. Raveau, Appl. Phys. Lett. **71**, 782 (1997).

[17] N.A. Pertsev, A.G. Zembilgotov, and A.K. Tagantsev, Phys. Rev. Lett. **80**, 1988 (1998).

[18] B. Mercey, P.A. Salvador, Ph. Lecoeur, W. Prellier, M. Hervieu, Ch. Simon, D. Chippaux, A.M. Haghiri-Gosnet, and B. Raveau, J. Appl. Phys. **94**, 2716 (2003).

[19] J. Kreisel, G. Lucazeau, C. Dubourdieu, M. Rosina, and F. Weiss, J. Phys.: Condens. Matter **14**, 5201 (2002).

[20] C.B. Eom, R.J. Cava, R.M. Fleming, Julia M. Phillips, R.B. van Dover, J.H. Marshall, J.W. P. Hsu, J.J. Krajewski, and W.F. Peck, Jr., Science **258**, 1766 (1992).

[21] T. Takeda and S. Ohara, J. Phys. Soc. Jpn. **37**, 275 (1974); O. Chmaissem, B. Dabrowski, S. Kolesnik, J. Mais, D.E. Brown, R. Kruk, P. Prior, B. Pyles, and J.D. Jorgensen, Phys. Rev. B **64**, 134412 (2001).

[22] The ionic radii of six-coordinate Ru^{4+} and Mn^{4+} are $r(\mathrm{Ru}^{4+})=0.62$ Å and $r(\mathrm{Mn}^{4+})=0.67$ Å. See R.D. Shannon, Acta Crystallogr., Sect. A: Cryst. Phys., Diffr., Theor. Gen. Crystallogr. **32**, 751 (1976).

[23] P.A. Salvador, A.M. Haghiri-Gosnet, B. Mercey, M. Hervieu, and B. Raveau, Appl. Phys. Lett. **75**, 2638 (1999).

[24] J. Verbeeck, O.I. Lebedev, G. Van Tendeloo, B. Mercey, Phys. Rev. B **66**, 184426 (2002).

[25] See http://ccp14.sims.nrc.ca/ccp/ccp14/ftp-mirror/diffax/pub/treacy/DIFFaX_v1807/

[26] B.D. Cullity, *Elements of X-Ray Diffraction* (Addison-Wesley, London, 1978), p. 102.

[27] E.E. Fullerton, I.K. Schuller, H. Vanderstaeten, and Y. Bruynseraede, Phys. Rev. B **45**, 9292 (1992).

[28] W. Prellier, Ph. Lecoeur, and B. Mercey, J. Phys.: Condens. Matter **13**, R915 (2001).

[29] Q. Gan, R.A. Rao, C.B. Eom, J.L. Garrett, and Mark Lee, Appl. Phys. Lett. **72**, 978 (1998).

[30] I.C. Noyan, T.C. Huang, and B.R. York, Crit. Rev. Solid State Mater. Sci. **20**, 125 (1995).

[31] J. O'Donnell, M.S. Rzchowski, J.N. Eckstein, and I. Bozovic, Appl. Phys. Lett. **72**, 1775 (1990), R.A. Rao, D. Lavric, T.K. Nath, C.B. Eom, L. Wu, and F. Tsui, J. Appl. Phys. **85**, 4794 (1999).

[32] S.S. Kim, T.S. Kang, and J.H. Je, J. Appl. Phys. **90**, 4407 (2001).